



AFM study of organic ligand packing on gold for nanoparticle drug delivery applications

Lemoine, P., Dooley, C., Morelli, A., Harrison, E., & Dixon, D. (2022). AFM study of organic ligand packing on gold for nanoparticle drug delivery applications. *Applied Surface Science*, 574, 1-12. [151386]. <https://doi.org/10.1016/j.apsusc.2021.151386>

[Link to publication record in Ulster University Research Portal](#)

Published in:
Applied Surface Science

Publication Status:
Published: 01/02/2022

DOI:
[10.1016/j.apsusc.2021.151386](https://doi.org/10.1016/j.apsusc.2021.151386)

Document Version
Peer reviewed version

General rights

Copyright for the publications made accessible via Ulster University's Research Portal is retained by the author(s) and / or other copyright owners and it is a condition of accessing these publications that users recognise and abide by the legal requirements associated with these rights.

Take down policy

The Research Portal is Ulster University's institutional repository that provides access to Ulster's research outputs. Every effort has been made to ensure that content in the Research Portal does not infringe any person's rights, or applicable UK laws. If you discover content in the Research Portal that you believe breaches copyright or violates any law, please contact pure-support@ulster.ac.uk.

AFM study of organic ligand packing on gold for nanoparticle drug delivery applications

Patrick Lemoine*, Chris Dooley, Alessio Morelli, Emma Harrison, Dorian Dixon
NIBEC, Ulster University, Shore Road, Newtownabbey, BT37 0QB, UK

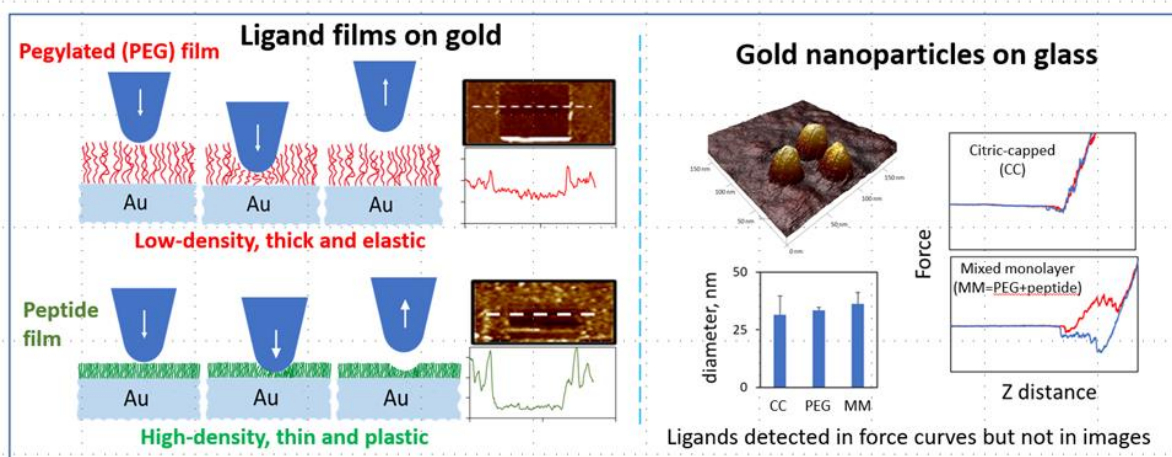
Corresponding author: Patrick Lemoine, p.lemoine@ulster.ac.uk

Keywords: Atomic Force Microscopy; gold; nanoparticle, functionalisation, drug delivery

Abstract

Gold nanoparticles (AuNPs) functionalized with polyethylene glycol (PEG) and peptide ligands are promising drug delivery vectors for use in cancer therapy. However, to control the interaction of the ligands with blood proteins and specific cell receptors, more needs to be known about the arrangement and properties of these grafted ligands. This issue is examined here principally with atomic force microscopy (AFM) for ligands grafted to both gold films and gold nanoparticles. Macro-level sessile drop measurements on the films indicate that, in dilute solutions, the PEG and peptide ligands exhibit similar affinity to the gold surface. However, at the nano-level, AFM experiments show differences in the morphology and cohesion of the adsorbed ligand films. Differences in tip/surface adhesion are also measured, indicative of variations of hydrophilicity for the top surface of these ligand films. Analysis of force-separation curves suggests a low packing density of PEG ligands. AFM investigations of functionalized AuNPs shows that the ligands improve dispersion and modify the tip/surface adhesion behaviour on the nanoparticles. However, AFM images of as-synthesised citric-capped and functionalized AuNPs gave similar nanoparticle diameters. Analysis of the AFM tip tapping on the AuNPs suggests that Tapping-AFM is not suitable for detection of low packing density ligands.

Keywords: gold nanoparticle, drug delivery, AFM microscopy, ligand, pegylation



1. Introduction

The conventional oral administration of therapeutic drugs and subsequent assimilation into the blood stream can result in over-dosages and poor targeting. The maximum tolerated dose of a therapeutic is generally limited by the toxic effects to healthy tissue. Hence, there is a great enthusiasm in using nanoparticles as agents to deliver drugs to a specific target, thus reducing dosage and side effects [1].

This is particularly true of cancer therapeutics as current drugs are not specific and generally damage adjacent healthy cells. In this context, there is a growing interest in using gold nanoparticles (AuNP) as targeted drug delivery systems for breast, prostate and pancreatic tumours for a number of reasons. AuNP are biocompatible. They are also photo-thermal agents as they absorb infrared radiation considerably more than the surrounding tissue, being denser. Hence if they can be made to enter cancer cells, using infrared radiation can result in producing heavy thermal damage to the cancer cells with much less to the surrounding tissue. Secondly, because of their high Z number, AuNP efficiently absorb X-rays, producing high energy electrons which can damage the DNA of cancer cells, in that sense, they are radiosensitizers [2], [3]. However, the AuNP needs to be functionalized with organic ligands -1/ to stabilise them and avoid aggregation, -2/ to escape non-specific protein adsorption (i.e. reduce immunogenicity), -3/ to maximize cell intake and, potentially, -4/ to attach drug molecules or other therapeutic agents such as genetic material. Surface functionalisation can also be used to enable endosomal escape once inside the target cell and to target the AuNP to a particular intracellular target such as the nucleus.

Attaching ligands of different lengths to a AuNP while ensuring that they all retain their functionality is a significant challenge. Generally, polyethylene-glycol (PEG) ligands are used to inhibit aggregation under *in vivo* conditions and are well-recognised immunosuppressive agents [4], [5]. The PEG ligands are typically bound to the Au surface by using thiolated PEG (PEG-SH). While PEGylated AuNP display an increased circulation time in the body compared to as-synthesised AuNP, they are largely inactive, in the sense that they do not naturally bond to cancer cell surface.

Peptides moieties, on the other hand, are designed to link to cell receptors and precipitate definite cell pathways, such as endocytosis or endosomal uptake. To date, functionalized AuNP have been mostly investigated in solution. Fourier transform infrared spectroscopy (FTIR), UV-visible absorption spectroscopy, dynamic light scattering (DLS) and ζ -potential measurements have shown an increase of particle's diameter upon functionalization by PEG and peptide ligands, as well as changes in surface charge and bonding environment [6], [7]. *In-vitro* measurements of many such functionalised AuNPs have demonstrated the effectiveness of PEG and peptides in both enhancing stability and avoiding any undesired immune response while enhancing specificity and cell uptake. For example, bio-responses on breast cancer cells indicate that such functionalized AuNP are indeed internalized and reduce cell survival rate following radio-therapy [8].

However, to fully realise the potential of such approaches requires, firstly, a knowledge of the arrangement and orientation of these PEG and peptide ligands on the nanoparticle. The peptide and PEG ligands differ in length and conformation and it is important to understand if the ligands are arranged randomly on the AuNP surface or if the two ligand types are segregated into islands. This arrangement will affect the ability of the peptide to interact directly with the cell surface. To image precisely this ligand arrangement is a hugely challenging task, attempted before using AFM [9] and also contested [10]. This has also been demonstrated using Transmission electron microscopy (TEM), decorating the organic ligands with tungsten oxide clustered anions [11], to improve electron contrast, although this is an indirect technique which may not image the pristine ligand arrangement. Instead, most studies have focused on solution measurements which only provide average values [12] and,

again, often indirect information. A more practical goal, which can inform on the ligand arrangement and which is not easily accessible from solution measurements, is to study the stiffness of the ligand shell. For NP with soft core, such as hydrogels, lipids, polystyrenes, this stiffness can impact on the NP delivery into the cellular cytoplasm [13-15]. For stiff AuNP with soft ligand shells, this is less likely. However, the stiffness of the soft ligand shell relates to the packing and arrangement of the ligand, hence is worth studying.

Hence, the approach taken in this investigation is to complement the analytical work carried out on AuNP colloidal solutions using atomic force microscopy (AFM) to investigate adsorbed AuNP as well as ligand films deposited on gold surfaces. The aim is -1/ to investigate the adsorption/affinity of PEG and peptide ligands on model gold films, 2/ to analyse, when feasible, the stiffness of the thin ligand shell and -3/ to carry out an AFM study of adsorbed functionalised-AuNP to obtain direct information on the attached ligand for singly detected particles; properties such as size, diameter and tip/surface forces on pull-off.

2. Materials and Methods.

2.1 Material and sample preparation procedures.

AuNP particles preparation

The AuNP were prepared via an adapted Turkevitch/Frens method [16] using sodium citrate as a reducing agent and labelled CC-AuNP. Some of these CC-AuNP were functionalized with a PEG-SH ligand and labelled PEG-SH-AuNP. Co-functionalisation was designed on two ligands, PEG-SH and a peptide, who have the same thiol-end to bond strongly to the AuNP's surface and was carried out using an established procedure [6,17] to have both ligands in equal measure on the AuNP's surface, an arrangement often described as the mixed monolayer (MM). The peptide used in this case was the receptor mediated endocytosis (RME) peptide, known to drive cell uptake. It can be attached to the AuNP surface using the thiol group of its terminal cysteine unit [6,7]. To achieve this, the CC-AuNP were first functionalized with PEG-SH up to 50% of the adsorbed ligand saturation, based on previous thermogravimetric measurements, and then subsequently functionalized with the RME-peptide to give the MM-AuNP. One should note that AuNP functionalised with RME-peptide only cannot be prepared as the corresponding colloidal dispersions are unstable, where the nanoparticles aggregate and then precipitate. UV-visible spectroscopy and FTIR spectroscopy confirmed the presence of the ligands on the AuNP [6,7]. The molecular structures of the ligands, sample names and properties are shown in table 1, together with measurement of hydrodynamic diameter (D_H) by DLS and ζ potential by electrophoretic spectroscopy.

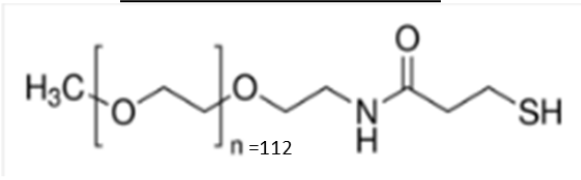
<u>Ligand</u>	<u>Molecular structure</u>		
PEG-SH (MW=5000 g/mol)			
RME-peptide (MW=2083 g/mol)	CKKKKKKSEDEYPYVPN		
	sample	D_H, nm (DLS)	ζ potential, mV (ELS)
	CC: AuNP	17.40 ± 0.20	-30.65 ± 1.5
	PEG-SH: AuNP	37.29 ± 0.37	-6.74 ± 0.5
	MM-RME: AuNP	38.23 ± 0.90	-4.4 ± 0.2

Table 1: Labelling, molecular structure of ligands and properties of AuNP. The amino-acid residues are labelled with the amino acid one letter code. D_H is the hydrodynamic diameter measured from dynamic light scattering and the ζ potential is measured from electrophoretic spectroscopy.

Ligand films and ligand solutions on gold substrates

The adequacy of planar gold to model the adsorption of PEG-SH ligands on AuNP has been discussed thoroughly in previous studies [18-20]. For a molecular weight (MW) of 5000 g/mol, a fully stretched PEG-SH chain would have a length $h \sim 30$ nm; taking C-C-C and O-C-O bond angles of, respectively 109° and 120°. However, whether in solution or grafted to a surface, polymer chains rarely adopt this extended configuration. In solution, polymer chains adopt a pseudo-Gaussian random coil conformation, characterised by the Flory radius R_F (in nm); the chain end-to-end distance; [21]

$$R_F = b^{2/5} \cdot a^{3/5} \cdot N^{3/5} \quad (1)$$

where a is the monomeric length (in nm), b is the Kuhn's length (in nm) and N the number of monomeric units. For the PEG-SH ligand used in this study (5000 g/mol; $N = 112$), $a = 0.28$ nm [22], $b = 0.72$ nm [21] give $R_F = 6.9$ nm.

Generally, for high surface curvature (small particle diameter) and/or very low packing density, the attached ligands adopt this same pseudo-Gaussian random coil conformation, sometimes labelled 'mushroom' conformation. If the ligand packing density Γ is larger than the critical value $\Gamma_c = R_F^{-2}$, 0.021 chain/nm² in the present case, the randomly coiled chains start to interact with each other and adopt a modified conformation, alike the bristles in a brush. From previous thermogravimetric (TGA) measurements on functionalized AuNP prepared with the same PEG-SH in the same conditions, we found a saturation concentration of PEG-SH on the AuNP of 14 wt.% [17]. Considering a AuNP diameter of 17.8-18.6 nm, as measured by TEM and DLS measurements [6,7], and the 5000 g/mol PEG-SH's MW, the expected PEG-SH chain surface density is $\Gamma = 1.05-1.1$ chain/nm² $> \Gamma_c$. Therefore, we believe that the PEG chains on the surface of the AuNP adopt the aforementioned brush-like conformation. The height of such tethered ligand films has indeed been calculated by minimising the two free energy terms [21,23], which are, as noted by Milner "stretching, which reduces the configurational entropy,

and overlapping with neighbouring chains, which reduces the energetically favorable contact with solvent molecules". The brush height derived from this calculation is:

$$h = \left(\frac{l}{3}\right)^{1/3} \cdot b^{2/3} \cdot a \cdot N = 17.5 \text{ nm} \quad (2)$$

In the case of the RME peptide, Pymol modelling shows it is in its fully-stretched rod-like configuration [7]. Counting 0.35-0.4 nm per residue [24] gives a length of 5.9-6.8 nm. Previous work [18,25] have also shown that, for AuNP diameter larger than 10 nm, the decreased curvature means that the chain packing reaches that of flat gold surfaces. We, therefore, believe that the gold film is an adequate model for our AuNP. As the RME peptide ligand is significantly shorter than the PEG-SH chain, it would take an even higher surface curvature (i.e. smaller AuNP) to stop ligand interactions, hence, here also the gold film represents a good model to study the interaction of RME-peptide with AuNP.

The ligand films were deposited on 2x2 cm² gold/glass substrates purchased from DRLI Inc. (10 nm Au on 5 nm Ti adhesion layer). Prior to depositing the ligand films, these gold substrates were cleaned by 10 min sonication in acetone, Isopropyl alcohol and then DI water. The DI water contact angle for these gold surfaces was 36°±5°. Hydrocarbon contaminants are known to increase this contact angle and previous studies [26] have shown that for contact angle values < 50°, the gold surface is deemed free of hydrocarbon contaminants. The chosen ligands are designed to form a strong covalent bond with the gold surface via the thiol group. Hence, the surface chemistry of the outer end of the ligands should be similar for the gold particles and the gold films.

These ligand films were prepared by immersing the 2x2 cm² gold substrates 8 hrs in approximately 10 ml of ligand solutions, followed by twice-rinsing with DI water (15 MΩ.m), then N₂-drying. This technique is more amenable to produce homogeneous monolayers of ligand film than drop casting which builds the film gradually by colloidal assembly from the contact line of the drop [27]. Initially, these ligand films were prepared from 7 μM solutions of PEG-SH and RME-peptide. Measuring the contact angle of these ligand solutions against the gold surface, no difference was found with DI water. In addition, the presence of the PEG-SH film could not be detected from the scratch measurements, as it gave a very elastic response. For these two reasons, we also prepared concentrated ligand solution at 200 μM. It should be noted that for all ligand films prepared by this immersion technique, the concentration of the ligand solution is not appreciably reduced by full coverage, hence the film formation results from the competing interactions between ligand, water and surface rather than a diffusion gradient towards the surface.

AuNP adsorption onto glass substrates

The nanoparticles CC-AuNP, PEG-SH-AuNP and MM-AuNP were adsorbed on glass slides, previously sonicated 10 min in acetone, then 10 min in IPA. The absence of hydrocarbon contaminant was again checked by measuring the DI water contact angle. These clean slides were immersed in dilute (7 μM) Au NP colloidal solutions for 15h. The glass slides were then twice rinsed with DI water (15 MΩ.m) and N₂-dried to remove excess AuNP, loosely bounded to the substrates.

2.2 Characterisation.

All AFM experiments were carried out with a Bruker DI3100 system using a series of AFM probes such as Bruker DNP Si₃N₄ Si probes (nominal spring constant $k=0.06$ N/m, resonant frequency $f=13$ kHz, tip radius $R=20$ nm), Budget Sensor ContAl Si probes (nominal $k=0.2$ N/m, $f=13$ kHz, $R=10$ nm), Bruker FESP Si probes (nominal $k=3$ N/m, $f=75$ kHz, $R=8$ nm) and Budget Sensors SHR150 Si probes (nominal $k=5$ N/m, $f=150$ kHz, $R=1$ nm). The DNP and ContAl probes were used exclusively in contact mode imaging (CAFM) whereas the SHR150 and FESP probes were also used in tapping mode imaging (TAFM). The measurements were performed in DI water or in air, with a ~ 60 % relative humidity. All images were acquired at 1 Hz scanning rate with 512x512 pixels, unless otherwise stated. Blind reconstruction on a standard sample was used periodically to monitor tip contamination or blunting [28]. The lever stiffness was calibrated using the Sader technique [29] and its sensitivity (in nm/V) was measured using a hard-sapphire sample. TAFM Imaging was carried out using gentle conditions; small amplitudes (20-50 nm) and high set points (60-80% of free amplitude, measured 100 nm above the engaged surface) as these represent good conditions to image very thin soft layers or loosely adsorbed AuNP. CAFM imaging used 0.2-0.4 V deflection set points (in air and in DI water). Image analysis of adsorbed AuNP were carried out using Image J or the Bruker Nanoscope 6 software. The particles are detected with a -5 nm height threshold with respect to the glass surface. Aggregates (large) and contaminants (small) can be filtered out and the average and standard errors are given for at least 20 particle measurements. One should note that in this paper, all AFM measurements on adsorbed AuNP are carried in TAFM in air as the particles are only loosely bound to the glass substrate and can be easily displaced by the AFM tip once immersed, as we observed many times. Obviously, the ligand arrangement on the AuNP surface may differ in air and in DI water and this represents a limitation of the study.

AFM scratch experiments on ligand films were carried out in air and DI water. The aim was to test the ligand attachment to the gold, the packing of the ligands, as well as its resistance to shear stresses. This requires a fairly stiff cantilever (~ 3 N/m) which resonates around 65-75 kHz. Unfortunately, the liquid cell which drives the acoustic modes usually used to perform tapping in liquid is not responsive to such high frequencies, hence the liquid measurements had to be done in CAFM mode. The following protocol was used. A $1 \times 0.5 \mu\text{m}^2$ rectangular area was scratched with a ~ 20 nN CAFM set point, with either DNP or ContAl probes, with more gentle CAFM imaging ($\sim 1-5$ nN set point) being done over a larger $2 \times 1 \mu\text{m}^2$ rectangular area before and after the scratch experiment. Control experiments were also done on the gold substrate to ensure that these scratch conditions did not result in a blunt tip or a scratched gold surface; i.e. no plastic deformation of the gold. Observation of a step height at the edge of the scratched area is a sign that some material has been permanently removed/deformed, usually measured from the height histogram. However, nothing can be said about the thickness as the ligand film may recover elastically. This may seem surprising as one may expect the AFM tip to 'scratch away' the soft ligand layer, however, in our experience, this rarely happens, and the step heights measured are always smaller than the film thickness.

Force curves, i.e. force versus relative z piezo-distance, were acquired for both air and in liquid conditions on at least 10 locations. The liquid environment has an obvious relevance to this investigation as, ultimately, these AuNP drug delivery systems are immersed in body fluids. Evidently, a PBS buffer or other media often used on cells/bacteria studies would be better to mirror a realistic biological environment. However, AFM measurements on very small adsorbed AuNP amongst a host of buffer adsorbates can be difficult to interpret. Hence, as in many published studies on AuNP [6-8,15], we choose DI water as the liquid of choice. However, the measurements in air are also instructive. It has been shown [30], that in air, the capillary meniscus force is the main contributor to the AFM pull-off force and that there is a direct relationship between hydrophilicity and AFM pull-off force. Hence, these measurements inform on the hydrophilicity of surface groups present on the top

surface of the ligand films. For the PEG-SH films, some force curve carried out with the soft DNP probes (nominal $k=0.06$ N/m) permitted to measure the elastic properties of the film. To that end, the F-z curve is transformed into a F-s curve, where the s is the tip/surface separation ($s=Z-d$, where d is the cantilever deflection). After having determined the contact point, a delicate operation for thin compliant films, the data is fitted to the Dimitriadis model [31], which considers the substrate effect, i.e a thin soft sample on a stiff substrate does not show the same deformation than a bulk soft sample of the same material.

AFM force curves on small AuNP are also challenging and were carried out on adsorbed AuNP using the Bruker 'point and shoot' routine on 10-20 AuNP, depending on the sample. The maximum applied force was 30 nN. The lateral drift was minimised by the XY feedback loop of the scanner. The adhesion force F_{adh} is defined as the pull-off force on retraction. These curves can also be replotted as force versus separation curve, which permits to extract the dissipation energy E_{diss} , defined as the area between the approach and retract segments of the F versus s curve. Considering that the ligands can have a variety of bonding environments over the surface of the particle, it is plausible that, depending on how the particle absorption takes place, and where the AFM tip precisely hits the AuNP, the force curves will record a range of tip/surface interactions. Hence, these measurements were carried out on at least 10 particles, with often several measurements per particle.

A CAM300 optical tensiometer system was also used to investigate the interaction between the ligand solutions on the gold surface. Pendant drops experiments were carried out to determine the surface tension of DI water, peptide solutions and PEG solutions, generally for drop volume of 6-8 μ l. For contact angle measurements, the sessile drop volume was kept above 5 μ l to minimise line tension effects [27]. The interfacial adhesion energy density W_a (in mJ/m^2) was calculated using:

$$W_a = \gamma_{LV} \cdot (1 + \cos\theta) \quad (3)$$

where θ is the contact angle and γ_{LV} is the solution surface tension (in mJ/m^2).

These experiments were only carried out for the concentrated ligand solutions (200 μ M) in order to measure detectable changes in surface tension and contact angle. Figure 1a summarises the essential points discussed above.

Statistical analysis of the data was performed using Microsoft Excel. Data in bar charts are presented as mean and standard error for at least 10 measurements. A Student t-test was used to compare pairs, for instance the PEG-SH and RME-peptide ligand solutions, or the various AuNP. The p-value was calculated assuming equal variance for both and using two tails. All results discussed in term of significant differences are those for based on the significance of variances, indicated as * for p-value < 0.05, ** for p-value < 0.01 and *** for p-value < 0.001.

3. Results and discussion.

3.1 Ligand films on gold substrates.

Figure 1 shows the results of the pendant drop (Fig. 1b) and sessile drop (Fig. 1c) experiments for the PEG-SH and RME peptide films prepared with 200 μ M solutions in DI water. The PEG-SH, with its amphiphilic backbone, is tensio-active and reduces the surface tension of DI water whereas the RME-peptide does not. The contact angle on gold of these two ligand solutions also differs. The compound effect of these two measurements is that, using eq.3, we find interfacial adhesion energy densities W_a

of $69.3 \pm 2.6 \text{ mJ/m}^2$ and $72.8 \pm 3.2 \text{ mJ/m}^2$ for the PEG-SH and the RME-peptide ligands, respectively (p -value < 0.01). Two observations can be made about this result. Firstly, at the macroscopic level, the two ligands have very similar affinity to gold, no statistically significant difference is found, a finding consistent with the ligand/gold interaction being dominated by the strong S-Au bond in both cases. Secondly, this behaviour is noted for a 200 μM concentration, that is a concentration where every ligand molecule is surrounded by 2.8×10^5 water molecules, hence in a solution that is still very dilute.

Figure 2 shows TAFM images in air of ligand films prepared by the immersion technique for the first batch, prepared with 7 μM solutions of PEG-SH (Fig. 2b) and RME-peptide (Fig. 2c). The gold substrate, also shown in Fig. 2a, is smooth with a very low RMS roughness value ($R_q=0.51 \text{ nm}$). All ligand films show full coverage and similarly low roughness values. The PEG-SH films exhibit a 'pitted', heterogeneous distribution of surface features. The lateral dimension of these pitted features varies from 30-100 nm, hence are much larger than the individual PEG-SH chains. This is indicative of an adsorption process where the ligand/surface interaction competes with the ligand/solvent interaction and is consistent with the good solubility of PEG chains. The absence of loose surface deposits is another indication of efficient rinsing of poorly attached ligands. By contrast, the RME-peptide displays smoother surfaces with adsorbed particulates (~ 50 -100 nm), which can be moved when exerting excessive contact force with the AFM tip. This would suggest loose deposits, which have not been shifted by the DI water rinsing step, hence less soluble than PEG-SH. Scratch experiments performed on these samples only resulted in an identifiable step height for the RME-peptide ($\sim 1.05 \text{ nm}$ high), as shown in Fig. 2e. The absence of step height for the PEG-SH film is indicative of an elastic response to the scratching load. It was hypothesised that at this low concentration (7 μM), the immersion time was insufficient to produce a dense PEG-SH layer; the PEG chains adopt a random coil conformation, which can somehow shield the SH bond of solubilized PEG ligands making the anchoring to the gold surface difficult. Hence the more concentrated solution was used (200 μM).

Figure 3 shows results for PEG-SH (Fig. 3a) and RME-peptide (Fig. 3b) ligand films prepared with these concentrated solutions, in this case imaged in CAFM mode in DI water. The RME-peptide layer is much rougher ($R_q= 1.63 \text{ nm}$ instead of 0.30 nm for PEG-SH) and presents obvious deposits, as observed in figure 2, but even more easily displaced by the AFM tip, hence loosely bound to the ligand layer. The PEG-SH layer has a similar 'pitted' nanostructure as when imaged in air in figure 2 but less pronounced. The absence of deposits for the PEG-SH ligand can be assigned to its lesser tendency to aggregate when prepared by an immersion technique.

In figure 4 are gathered results from scratch experiments on the samples prepared in concentrated solutions, carried out both in air and in DI water for the PEG-SH (Fig. 3a) and RME-peptide (Fig.3b) ligands. In this case, the scratching resulted in a step height trench for both ligand films, although the RME-peptide resulted in larger step height (in air, $\Delta h=-1.2 \text{ nm}$ for PEG-SH and $\Delta h=- 2.1 \text{ nm}$ for RME-peptide). For a ligand film on a hard surface, the observation of a residual scratch depth can be indicative of delamination, unlikely to happen in the present case as both ligands bond to gold via strong covalent thiol bonds. Residual scratch depth can also be due to plastic deformation of the ligand film. Previous AFM scratching studies on thiol-terminated self-assembled monolayers on gold substrates have indeed shown that these chains resist remarkably well the pressure under the indenter tip, with compressed chains supporting the load even when the gold plastically deformed [32]. A plastic deformation in the ligand film corresponds to a change in the chain packing density. In compression, this is more likely to happen for a tightly packed molecular system than for loosely bound chains. Generally, chain packing density decreases with chain length [20-22]. Having established above that, the RME peptide chains (5.9-6.8 nm) are much shorter than the PEG-SH chains ($\sim 17.5 \text{ nm}$), one would expect denser peptide packing on the gold surface. The inter-chain

interactions are also relevant to this discussion. The RME-peptide ligand is made off 17 amino-acid residues. The thiol bond attached to the gold surface is situated on the protein's terminal cystine residue. Following this cysteine residue, there are 10 amino acid residues with either charged or polar side chains (i.e. KKKKKKSEDE), followed by 5 amphiphilic and/or hydrophobic residues and a final hydrophilic asparagine (N) residue. In this rod-like configuration, there could be strong dipole-dipole attractive interactions between these side groups, particularly the six consecutive lysine residues, as polylysine is known to adsorb in brush-like configuration [33]. Indeed, dense chain packing with the rod-like peptide chains orienting more or less perpendicular to the gold surface has been observed for other oligomeric ligands such as alkylated organic ligands [34]. Incidentally, these same attractive interactions between peptide chains can be responsible for the observed small adsorbates seen on the RME peptide films in figure 3 and 4. For the PEG-SH used in this study, as discussed above, the likely brush configuration would lead to a height of 17.5nm (eq. 2). In this non-optimized packing configuration, the long PEG-SH chains are not fully-stretched, rather partially coiled with possibly some entanglement between chains, which could indeed result in the observed elastic behaviour. This would be consistent with our previous DLS results on PEG-SH functionalized AuNP adopting an extended random coil configuration [17].

Figure 5 shows force curves obtained in air and in DI water of the two ligand films. The force and displacement resolutions here are not sufficient to measure the deformation in the ligand film, the aim is solely to study the pull-off, and corresponding pull-off energy while retracting the tip from the ligand film. In air, the RME peptide shows the largest pull off force/ pull-off energy, reported in the figure. As discussed earlier, the AFM pull-off force in moist air is a measure of surface hydrophilicity, in this case the surface character of the ligand film's external surface. For PEG-SH, anchoring on the gold at the SH end would bury the polar carbonyl group and expose the opposite methyl end, an unfavourable scenario to promote hydrophilicity. By contrast, the dense RME peptide ligand layer, also bonded at the SH end, has a packing of lysine residues ending with the polar asparagine residue, hence a hydrophilic external surface. These interpretations can be corroborated by the friction images in figure 4. Previous studies in ambient atmosphere on self-assembled organic monolayers, using end groups with specific hydrophilic or hydrophobic surface character, have shown that the friction force can be correlated to the surface characters of the tip and surface [35]. Figure 4 shows that, for the PEG-SH film in air, there is a strong positive friction contrast ($\Delta f = +28$ mV), a result consistent with a hydrophobic PEG-SH external surface, a hydrophilic gold surface and a hydrophilic Si/SiO₂ tip surface. For the RME peptide film in air, there is no such friction contrast ($\Delta f = 0$ mV), as the AFM tip, external ligand film's surface and gold's surface are all hydrophilic. In DI water, the absence of capillary meniscus and the low lateral force sensitivity of the AFM make these friction contrasts a lot smaller and no apparent trend can be observed. For the force curves obtained in DI water, figure 5 shows much reduced pull off forces and energies because of the absence of capillary meniscus.

An attempt to measure the PEG-SH ligand film compression is shown in figure 6, here using a softer AFM cantilever (0.06 N/m) at a low force set point (< 1nN). Figure 6a shows exemplar AFM approach force curves (F vs Z) for the gold substrate and the PEG-SH film. For the gold surface, an attractive pull-in of ~ 260 pN is observed, after this, the cantilever force increases linearly, indicating minimal surface deformation. For the PEG-SH layer, no initial attraction is observed, and the force increases in a parabolic manner, a trend consistent with a mechanical response. In figure 6b, nine experimental force separation curves (red dots) are shown for the PEG-SH film. The force increases in a parabolic manner for a 15-20 nm separation distance, after which the trend is again linear. This mechanical response seems consistent with the estimated 17.5 nm ligand thickness. The insert shows the corresponding average deformation curve where the separation has been offset to the surface contact position, shown with dashed lines. The fit to the Dimitriadis model [31] is shown in figure 6b. The resulting

Young modulus value is very low ($E = 45 \pm 5$ kPa, $R^2 = 0.954$), indeed much lower than that measured previously by Huang *et al* for a PEG film with a similar 5000g/mol molecular weight [36] ($E = 2570 \pm 680$ kPa). One should note that these E measurements on soft thin samples are not straightforward, the challenge in determining the contact point being noted above. Also, the fact that such a thin film model is only valid for indentation depths smaller than the film thickness (here fitted only for the first 10 nm of indentation) also limits the accuracy of the fit. Nonetheless, the large discrepancy between our result and Huang's may originate from the different PEG chain used (PEG-silane for ref. 36, PEG-SH here), difference in polydispersity or, more crucially, a difference in chain entanglement and chain density which would strongly affect the stiffness response of the film. For instance, systems with characteristically low chain density, such as PEG hydrogels, display a similar E value ($E \sim 30$ kPa) when probed by AFM [35]. This low stiffness value is also consistent with the repulsive interactions between PEG chains mentioned noted by Israelachvili [37]. Finally, as noted in the introduction, a soft hydrophobic ligand can facilitate cell uptake, which is advantageous for drug delivery applications

3.2 AuNPs adsorbed on glass and Si substrates.

Figure 7 shows TAFM images of AuNPs adsorbed onto a glass substrate. The AuNPs are readily distinguishable from residual contamination on the glass substrates, particularly from the cross-sectional traces which shows a consistent ~ 13 - 17 nm height for all AuNP, in agreement with TEM diameter measurements [7]. The figure also indicates that aggregates seen on the adsorbed CC-AuNP sample are absent on the images of the adsorbed functionalized particles, demonstrating that the ligands help disperse these AuNP particles. One also notes the low packing density of the AuNPs on the surface; 3 - $10 \mu\text{m}^{-2}$ for CC-AuNP and 10 - $30 \mu\text{m}^{-2}$ for PEGSH-AuNP and MM-AuNP. We also report the ζ potential values, as measured by electrophoretic light scattering for these colloidal systems, all negative. One notes that, as the glass surface in water has a negatively charged surface [38], there is an approximate inverse relationship between AuNP surface density and ζ potential, as one would expect. However, as the particles are always detected, even for the highly repulsive electrostatic interaction between CC-AuNP and the glass surface, there must be other more dominating interactions, attractive in nature (Van der Waals, depletion or H-bonding, etc.), between the AuNP on the glass surface.

To detect the ligands on the surface of the particles, gentle tapping conditions and fresh and sharp tips were used. A parametric study was undertaken to investigate the effect of imaging parameters such as excitation frequency, drive amplitude, feedback gains and tapping set point, all known to affect the resolution [39]. It was found that the studied range of imaging parameters did not affect significantly the TAFM images of these AuNP particles. No hysteresis artefacts were observed in the amplitude force curves, however, the ~ 5 - 10 mV amplitude noise level corresponds to a 0.5 - 1 nm uncertainty and probably represents a limitation for detecting the ligand. Higher magnification TAFM images are shown in figure 8a for the CC-AuNP, PEGSH-AuNP and MM-AuNP. The particle's diameters and heights, detected as described in section 2/, are presented in figure 8b. The table in Figure 8c gathers p-values from pair-comparisons and indicates that TAFM did not detect any statistically significant differences in either diameter or height for the three different AuNP. The average measured particle diameter for the three different AuNP is 33.6 ± 2.4 nm. With an 8 nm tip radius, this gives a deconvoluted 16.1 ± 1.5 nm AuNP diameter, very close to the measured averaged particle height (15.8 ± 1.0 nm) and also close to value measured by TEM measurements [7], which only detect the gold core.

Figure 9 displays force-separation curves for the three AuNP samples obtained in air. There are clear differences in pull-off force $F_{\text{adh.}}$ and dissipation energies $E_{\text{diss.}}$, as indicated in the figure, with the MM-

AuNP displaying significantly larger values. Considering the equally large values measured for the RME-peptide film in air (Fig.5), it is possible that the RME-peptide molecules are tightly packed in clusters, interspaced with less dense PEG-SH regions, on the surface of the MM-AuNP particle. Israelachvili [37] noted that the repulsive interactions between PEG chains is known to favour PEG/protein interactions which would increase energy dissipation following the tip retraction, as observed in figure 9.

It seems, therefore, that TAFM as used in this study is not capable of detecting the ligands from the measurement of particle dimensions. Scanning the literature, one finds many studies where AFM microscopy can resolve biomolecular chains adsorbed on atomically flat substrates, however, to the best of the author's knowledge, successful imaging of molecular ligands attached to nanoparticles are very scarce [9,40] and, as previously noted, sometimes contested [10]. Generally, to detect a thin and soft organic layer onto a hard surface, one tends to apply a low force. This is based on the many nanoindentation and AFM investigations of thin film systems which attempt to take into account this substrate effect [41-43] to extract intrinsic mechanical properties. However, these studies are based on a continuum description of the nanomechanical behaviour; i.e. the material tested is homogeneous down to the nanoscale. In the case of nanoparticles functionalized with polymeric ligands, this description is inadequate and one needs to consider the packing density of the ligands on the AuNP particle. This chain packing density was estimated for the PEG-SH ligand, as discussed earlier ($\Gamma = 1.01$ chain/nm²) and this can help gauge the number of chains sensed by the AFM tip based on the estimation of the tip/surface force F_{ts} and, using contact mechanics, the tip/surface contact area. For TAFM imaging conditions, one needs to consider the average force $\langle F_{ts} \rangle$ during the cantilever oscillations. This $\langle F_{ts} \rangle$ value has been calculated for amplitude-modulation TAFM imaging [44], the details of the calculations are given in appendix A. For the conditions used in the TAFM images of figure 10, one finds $\langle F_{ts} \rangle = 0.32$ nN. The relationship between the force and the contact radius a is given by the chosen contact mechanics model. Again, these models (see appendix B) are generally based on a continuum description of the tip/surface elastic deformation. The contact radius a and the chain density Γ give the number of chains n sensed by the AFM tip. For the PEGSH-AuNP examined in the conditions of figure 8, the value of n is 0.4 for the Hertz model, 5.5 for the DMT model and ~ 10 for the JKR model.

Clearly, the larger force used in the force-separation curves of figure 9 (~ 30 nN) would result in many more ligand chains being probed by the tip and explain why differences are seen between the various particles in figure 9 but not in figure 8. This analysis indicates that imaging low density organic ligands using amplitude modulation TAFM is challenging as the use of gentle conditions at high set point results in sampling very few polymeric chains. More sensitive schemes using, for instance, frequency modulation [45], higher harmonics [46] or bimodal operation [47]. would be of benefit to investigate ligand arrangement on the surface of nanoparticles for drug delivery applications.

4. Conclusions.

The interactions of PEG and peptide ligands with gold surfaces and gold nanoparticles were studied by AFM microscopy. Pendant and sessile drop measurements showed that the two ligands exhibit similar affinity to the gold surface at the macro-scale. However, at the nano-level, TAFM experiments show differences in the morphology, continuity and cohesion of the adsorbed ligand films. Differences in tip/surface adhesion in water are also measured. The analysis of compression experiments at low

force gives a 45 kPa Young modulus for the PEG-SH layer, indicative of a low chain packing density in the film. TAFM microscopy of the functionalized AuNP shows that the ligands improve dispersion and modify the tip/surface adhesion behaviour on the nanoparticles. However, TAFM images of citric-capped and functionalized AuNP were similar. Analysis of the AFM tip tapping on the AuNP suggests the TAFM detection of low packing density ligands on gold nanoparticles is a challenging task.

CRedit authorship contribution statement

P. Lemoine: Conceptualization, methodology, validation, formal analysis, investigation, writing original manuscript. **C. Dooley:** investigation, **A. Morelli:** investigation, **Emma Harrison:** investigation, **D. Dixon:** Conceptualization, methodology, resources, funding acquisition. All authors contributed to reviewing and editing the manuscript.

Declaration of Competing Interest

The authors declare that they have no known competing financial interests or personal relationships that could have appeared to influence the work reported in this paper.

Acknowledgements.

This work was supported and funded by the Department of the Economy (DeC) Northern Ireland.

Appendix A

The aim is first to calculate the frequency response of the cantilever's free oscillations. We are considering that the tip is some distance away from the surface (i.e. 100 nm), where tip/surface forces are negligible and where the only damping is hydrodynamical. The motion of the cantilever can be described using forced oscillation concepts [MK]. In the present case of amplitude modulation TAFM excitation, the cantilever's base is excited directly by a harmonic displacement imposed by the piezo-element of its holder. A schematic of this dynamic system is shown in figure A1.

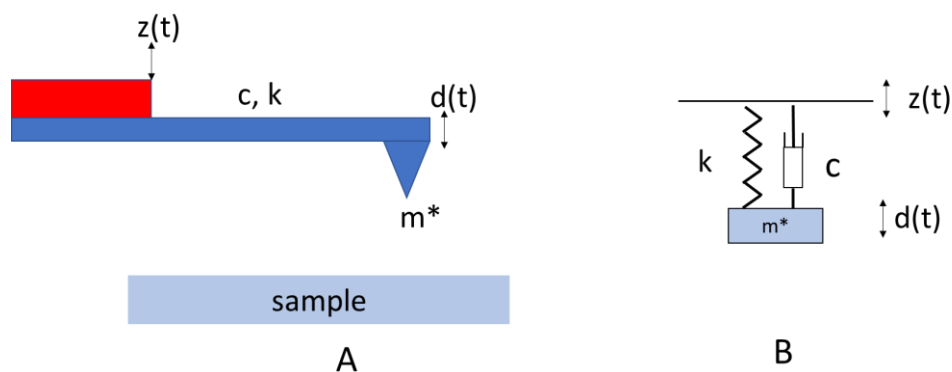


Figure A1: Free oscillation of a TAFM lever: A/ schematic and B/ dynamic model

The cantilever, of spring constant k , is considered as a point-mass spring system of effective mass m^* , subjected to the cantilever's restoring force and to the air's viscous drag, characterised by the damping coefficient c . If d and z represent the dynamic oscillations of the AFM tip and driving cantilever base oscillation, respectively, we have

$$m_* \cdot d'' = -k \cdot (d - z) - c \cdot (d' - z') \quad \text{eq. A1}$$

Rearranged as;

$$m_* \cdot d'' + c \cdot d' + k \cdot d = c \cdot z' + k \cdot z \quad \text{eq. A2}$$

This forced oscillator has a natural angular frequency $\omega_n = 2\pi \cdot f_n = 2\pi \cdot (k/m_*)^{1/2}$, damping ratio $\beta = c/(2m_* \cdot \omega_n)$ and the right hand term represents the excitation. Examining the harmonic steady-state regime, the complex solutions, in polar form, are;

$$z(t) = z_0 \cdot e^{i\omega t} \quad \text{eq. A3}$$

$$d(t) = d_0 \cdot e^{i\omega t} \cdot e^{-i\varphi} \quad \text{eq. A4}$$

The quantity ω is the driving angular frequency ($\omega = 2\pi \cdot f$, where f is the driving frequency). Differentiating, and feeding eq. A3 and A4 into eq. A2, we can calculate the peak to peak amplitude of oscillation d_0 ; i.e. the absolute value, or modulus, of the complex $d(t)$;

$$d_0 = \frac{z_0 \cdot \sqrt{1 + 4b\beta^2}}{\sqrt{(1-b)^2 + 4b\beta^2}} \quad \text{eq. A5}$$

In this equation b is the square of the frequency ratio; $b = (\omega/\omega_n)^2 = (f/f_n)^2$, and the damping ratio β represents the normalised effect of the system's damping coefficient c but also relates to the width of the resonance peak via the Q factor;

$$\beta = \frac{c}{2.m_s.\omega_n} = \frac{1}{2Q} \quad \text{eq. A6}$$

Applying this to the conditions used in figure 7; i.e. $f=66.3$ kHz, $f_n=66.6$ kHz and $Q=200$ gives $b=0.991$ and $\beta=0.0025$, hence $4.b.\beta^2=2.48 \times 10^{-5} \ll 1$. Equation A5 can be therefore simplified to;

$$d_0 = \frac{z_0}{\sqrt{(1-b)^2 + 4b\beta^2}} \quad \text{eq. A7}$$

Equation A6 is the starting point of most analytical analysis of TAFM vibrations, usually written as if an harmonic force of amplitude F_0 and frequency f was directly applied to the tip;

$$d_0 = \frac{F_0/k}{\sqrt{(1-b)^2 + 4b\beta^2}} \quad \text{eq. A8}$$

In the case of figure 7, the free oscillation amplitude $d_0 = 27$ nm gives an harmonic force amplitude $F_0=0.78$ nN for the b and β values quoted above. With this oscillation amplitude, it can be assumed that the average tip/surface force $\langle F_{ts} \rangle$ is only active at the turning point of the oscillation, near the sample. In this condition, the tapping amplitude d can be calculated [48];

$$d = d_0 \cdot \sqrt{1 - 4 \left(\frac{\langle F_{ts} \rangle}{F_0} \right)^2} \quad \text{eq. A9}$$

Rearranged as;

$$\langle F_{ts} \rangle = \frac{1}{2} \cdot F_0 \sqrt{1 - \left(\frac{d}{d_0} \right)^2} \quad \text{eq. A10}$$

This gives a force $\langle F_{ts} \rangle = 0.32$ nN. This constitutes the starting point for calculating the tip/surface contact radius, using a contact mechanics model (i.e. appendix B).

Appendix B

Contact mechanics models are continuum mechanic descriptions of tip/surface contact, for an AFM tip of Young modulus E_{tip} Poisson ratio ν_{tip} and a surface of Young modulus E and Poisson ratio ν . The description given here is for a sphere of radius R (the tip) applying a force F on a flat (the surface). In the Hertz contact model, the contact radius a and surface deformation def can be calculated as;

$$a = \left[\frac{3FR}{4E_r} \right]^{1/3} \quad \text{eq. B1}$$

$$def = \frac{a^2}{R} \quad \text{eq. B2}$$

Where E_r is the reduced modulus;

$$E_r = \left(\frac{1-\nu_{tip}^2}{E_{tip}} + \frac{1-\nu^2}{E} \right)^{-1} \quad \text{eq. B3}$$

As the Hertz model does not take into account adhesion forces, other models have been developed, the most commonly used ones being the Johnson-Kendall-Roberts (JKR) and the Derjaguin-Muller-Toporov (DMT) model [48]. In the JKR model, on approach, the adhesion forces deform the surface and bring it into contact; i.e. there is a contact area at zero applied load. The

adhesion force F_a , can be measured from the pull-off value during retraction on a force curve. The equations for this JKR model are;

$$F_a = 3.\pi.R.\gamma \quad \text{eq. B4}$$

$$d_a = \left(\frac{\pi^2 .R.\gamma^2}{3.E_r} \right)^{\frac{1}{3}} \quad \text{eq. B5}$$

The deformation def can be calculated as a function of the relative force $f=F/F_a$

$$\frac{def}{d_a} = 3(f + 2 + 2\sqrt{1+f})^{\frac{2}{3}} - 4(f + 2 + 2\sqrt{1+f})^{\frac{1}{6}} \quad \text{eq. B6}$$

In the DMT model, the effect of adhesion forces is only taken into account insofar as the applied force F in eq. B1 of the Hertz model is replaced F_{DMT} ;

$$F_{DMT} = F + 4.\pi.R.\gamma \quad \text{eq. B7}$$

Figure captions

Table 1: Labelling, molecular structure of ligands and properties of AuNP. The amino-acid residues are labelled with the amino acid one letter code. D_H is the hydrodynamic diameter measured from dynamic light scattering and the ζ potential is measured from electrophoretic spectroscopy.

Figure 1: Contact angle and pendant drop experiments for the ligand solutions : a) schematics and equations, b) surface tension results and c) contact angle results on the gold surface.

Figure 2: TAFM height images in air of ligand layers from dilute solutions (7 μM): a) gold substrate, b) PEG-SH 8hrs, c) RME-peptide 8hrs, d) RME-peptide 8 hrs with scratched area, e) Height histogram from d) showing 1.05 nm step height. The 400 nm scale bar and 10 nm height scale are for all images.

Figure 3: 1 μm CAFM height images in DI water of ligand layers from concentrated solutions (0.2 μM): a/ PEG-SH ($R_q = 0.30$ nm) and b/ RME-peptide ($R_q = 1.63$ nm). 200 nm marker bar and 4 nm height scale are the same for both images.

Figure 4: 2 μm CAFM height and friction images of ligand layers from concentrated solutions (0.2 μM) obtained in air and in DI water: a/ PEG-SH and b/ RME-peptide. The contrast between the scratched and unscratched area is shown in the images for the height (Δh) and friction (Δf) signals. Scale bar, shown for all image is 400 nm.

Figure 5: Average AFM force-separation curves in air and in DI water for ligand films on gold; RME peptide and PEGSH obtained in air and in DI water prepared at 200 μM . The adhesion pull-off force (in nN) and energy dissipation (in aJ) are also shown in the curves.

Figure 6: a/ Force curves obtained in DI water at low force for gold and the PEGSH film prepared at 200 μM , b/ Force separation curves and, insert, force-indentation curve with fit of the Dimitriadis model (ref 31) to take into account the substrate effect. The calculated low Young modulus value is indicative of a film with low chain density and entanglements.

Figure 7: 4 μm TAFM images in air for of glass substrate and adsorbed AuNPs. Cross-sectional traces are shown below the images. Marker bar= 200 nm in both main images and inserts. The 1 μm cross-sections, all with a 25 nm vertical scale, are across significant features; i.e. contaminants for the glass, AuNP for the other samples.

Figure 8: a/ 500nm TAFM images in air for CC-AuNP, PEGSH-AuNP and MM-AuNP adsorbed on glass obtained with optimised imaging conditions. b/ Corresponding histograms for particle heights and diameters and c/ table of student t-test p-values for 'pair comparisons', in red for diameter and blue for height, showing no statistical differences between the three samples (i.e. p-values > 0.05)

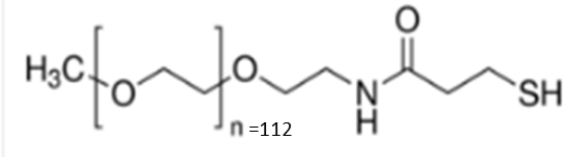
Figure 9: Representative AFM force-separation curves for CC-AuNP, PEGSH-AuNP and MM-AuNP

References

- [1] S. Gelperina, K. Kisich, M.D. Iseman, L. Heifets, The potential advantages of nanoparticle drug delivery systems in chemotherapy of tuberculosis, *Am. J. Respir. Crit. Care Med.* 172 (2005) 1487-1490.
- [2] H.N. McQuaid, M.F. Muir, L.E. Taggart, S.J. McMahon, J.A. Coulter, W.B. Hyland, S. Jain, K.T. Butterworth, G. Schettino, K.M. Prise, D.G. Hirst, S.W. Botchway, F.J. Currell, Imaging and radiation effects of gold nanoparticles in tumour cells, *Sci. Rep.* 6 (2016).
- [3] L. Tong, Q. Wei, A. Wei, J.-. Cheng, Gold nanorods as contrast agents for biological imaging: Optical properties, surface conjugation and photothermal effects, *Photochem. Photobiol.* 85 (2009) 21-32.
- [4] P. Mishra, B. Nayak, R.K. Dey, PEGylation in anti-cancer therapy: An overview, *Asian J. Pharm. Sci.* 11 (2016) 337-348.
- [5] J.V. Jokerst, T. Lobovkina, R.N. Zare, S.S. Gambhir, Nanoparticle PEGylation for imaging and therapy, *Nanomedicine.* 6 (2011) 715-728.
- [6] E. Harrison, J.R. Nicol, M. Macias-Montero, G.A. Burke, J.A. Coulter, B.J. Meenan, D. Dixon, A comparison of gold nanoparticle surface co-functionalization approaches using Polyethylene Glycol (PEG) and the effect on stability, non-specific protein adsorption and internalization, *Mater. Sci. Eng. C.* 62 (2016) 710-718.
- [7] E. Harrison, J.W.J. Hamilton, M. Macias-Montero, D. Dixon, Peptide functionalized gold nanoparticles: The influence of pH on binding efficiency, *Nanotechnology.* 28 (2017).
- [8] J.R. Nicol, E. Harrison, S.M. O'Neill, D. Dixon, H.O. McCarthy, J.A. Coulter, Unraveling the cell-type dependent radiosensitizing effects of gold through the development of a multifunctional gold nanoparticle, *Nanomed. Nanotechnol. Biol. Med.* 14 (2018) 439-449.
- [9] Q. Ong, Z. Luo, F. Stellacci, Characterization of Ligand Shell for Mixed-Ligand Coated Gold Nanoparticles, *Acc. Chem. Res.* 50 (2017) 1911-1919.
- [10] J. Stirling, I. Lekkas, A. Sweetman, P. Djuranovic, Q. Guo, B. Pauw, J. Granwehr, R.L. Lévy, P. Moriarty, Critical assessment of the evidence for striped nanoparticles, *PLoS ONE.* 9 (2014).
- [11] Y. Wang, O. Zeiri, A. Neyman, F. Stellacci, I.A. Weinstock, Nucleation and island growth of alkanethiolate ligand domains on gold nanoparticles, *ACS Nano.* 6 (2012) 629-640.
- [12] G. Stan, F.W. Delrio, R.I. MacCuspie, R.F. Cook, Nanomechanical properties of polyethylene glycol brushes on gold substrates, *J Phys Chem B.* 116 (2012) 3138-3147. doi:10.1021/jp211256f.
- [13] J. Zhao, M.H. Stenzel, Entry of nanoparticles into cells: The importance of nanoparticle properties, *Polym. Chem.* 9 (2018) 259-272. doi:10.1039/c7py01603d.
- [14] S. Wang, H. Guo, Y. Li, X. Li, Penetration of nanoparticles across a lipid bilayer: Effects of particle stiffness and surface hydrophobicity, *Nanoscale.* 11 (2019) 4044-4052. doi:10.1039/c8nr09381d.
- [15] X. Banquy, F. Suarez, A. Argaw, J. Rabanel, P. Grutter, J. Bouchard, P. Hildgen, S. Giasson, Effect of mechanical properties of hydrogel nanoparticles on macrophage cell uptake, *Soft Matter.* 5 (2009) 3984-3991. doi:10.1039/b821583a.
- [16] J. Turkevich, P.C. Stevenson, J. Hillier, A study of the nucleation and growth processes in the synthesis of colloidal gold, *Discussions of the Faraday Society.* 11 (1951) 55-75.

- [17] J. Manson, D. Kumar, B.J. Meenan, D. Dixon, Polyethylene glycol functionalized gold nanoparticles: The influence of capping density on stability in various media, *Gold Bull.* 44 (2011) 99-105.
- [18] C. Vericat, G.A. Benitez, D.E. Grumelli, M.E. Vela, R.C. Salvarezza, Thiol-capped gold: From planar to irregular surfaces, *J Phys Condens Matter.* 20 (2008). doi:10.1088/0953-8984/20/18/184004.
- [19] H. Liu, T.L. Doane, Y. Cheng, F. Lu, S. Srinivasan, J. Zhu, C. Burda, Control of Surface Ligand Density on PEGylated Gold Nanoparticles for Optimized Cancer Cell Uptake, *Part. Part. Syst. Charact.* 32 (2015) 197-204. doi:10.1002/ppsc.201400067.
- [20] U. Dahal, Z. Wang, E.E. Dormidontova, Hydration of Spherical PEO-Grafted Gold Nanoparticles: Curvature and Grafting Density Effect, *Macromolecules.* 51 (2018) 5950-5961. doi:10.1021/acs.macromol.8b01114.
- [21] G. Emilsson, R.L. Schoch, L. Feuz, F. Hook, R.Y.H. Lim, A.B. Dahlin, Strongly Stretched Protein Resistant Poly(ethylene glycol) Brushes Prepared by Grafting-To, *Acs Applied Materials & Interfaces.* 7 (2015) 7505-7515. doi:10.1021/acsami.5b01590.
- [22] F. Oesterhelt, M. Rief, H.E. Gaub, Single molecule force spectroscopy by AFM indicates helical structure of poly(ethylene-glycol) in water, *New Journal of Physics.* 1 (1999) 6.1. doi:10.1088/1367-2630/1/1/006.
- [23] S.T. Milner, Polymer Brushes, *Science.* 251 (1991) 905-914. doi:10.1126/science.251.4996.905.
- [24] R.K. Ainarapu, J. Brujic, H.H. Huang, A.P. Wiita, H. Lu, L. Li, K.A. Walther, M. Carrion-Vazquez, H. Li, J.M. Fernandez, Contour length and refolding rate of a small protein controlled by engineered disulfide bonds, *Biophys. J.* 92 (2007) 225-233. doi:10.1529/biophysj.106.091561.
- [25] W. Chen, R. Cordero, H. Tran, C.K. Ober, 50th Anniversary Perspective: Polymer Brushes: Novel Surfaces for Future Materials, *Macromolecules.* 50 (2017) 4089-4113. doi:10.1021/acs.macromol.7b00450.
- [26] T. Smith, *J Colloid Interface Sci.* 75 (1980) 51. doi:10.1016/0021-9797(80)90348-3.
- [27] P.K. Yadav, P. Lemoine, Comparative Sessile Drop and Dip Pen Nanolithography Investigation for Various Hydrophilic Ink/Surface Systems, *Journal of Nanoscience and Nanotechnology.* 12 (2012) 60-67. doi:10.1166/jnn.2012.5731.
- [28] L.S. Dongmo, J.S. Villarrubia, S.N. Jones, T.B. Renegar, M.T. Postek, J.F. Song, Experimental test of blind tip reconstruction for scanning probe microscopy, *Ultramicroscopy.* 85 (2000) 141-153. doi:10.1016/S0304-3991(00)00051-6.
- [29] J.E. Sader, J.W.M. Chon, P. Mulvaney, Calibration of rectangular atomic force microscope cantilevers, *Rev. Sci. Instrum.* 70 (1999) 3967-3969.
- [30] A. Rana, A. Patra, M. Annamalai, A. Srivastava, S. Ghosh, K. Stoerzinger, Y.-. Lee, S. Prakash, R.Y. Jueyuan, P.S. Goohpattader, N. Satyanarayana, K. Gopinadhan, M.M. Dykas, K. Poddar, S. Saha, T. Sarkar, B. Kumar, C.S. Bhatia, L. Giordano, S.-. Yang, T. Venkatesan, Correlation of nanoscale behaviour of forces and macroscale surface wettability, *Nanoscale.* 8 (2016) 15597-15603.
- [31] E.K. Dimitriadis, F. Horkay, J. Maresca, B. Kachar, R.S. Chadwick, Determination of elastic moduli of thin layers of soft material using the atomic force microscope, *Biophys. J.* 82 (2002) 2798-2810. doi:10.1016/S0006-3495(02)75620-8.

- [32] R.W. Carpick, M. Salmeron, Scratching the surface: Fundamental investigations of tribology with atomic force microscopy, *Chem. Rev.* 97 (1997) 1163-1194.
- [33] J. Wu, Y. Chen, Y. Wang, H. Yin, Z. Zhao, N. Liu, M. Xie, Y. Chen, Poly-L-lysine brushes on magnetic nanoparticles for ultrasensitive detection of Escherichia coli O157: H7, *Talanta*. 172 (2017) 53-60. doi:10.1016/j.talanta.2017.05.035. [14] L.S. Dongmo, J.S. Villarrubia, S.N. Jones, T.B. Renegar, M.T. Postek, J.F. Song, Experimental test of blind tip reconstruction for scanning probe microscopy, *Ultramicroscopy*. 85 (2000) 141-153
- [34] M.D. Porter, T.B. Bright, D.L. Allara, C.E. Chidsey, Spontaneously Organized Molecular Assemblies. 4. Structural Characterization of n-Alkyl Thiol Monolayers on Gold by Optical Ellipsometry, Infrared Spectroscopy, and Electrochemistry, *J. Am. Chem. Soc.* 109 (1987) 3559-3568.
- [35] Kolewe, Kristopher W., "Structure-Property Relationships of Polymer Films and Hydrogels to Control Bacterial Adhesion" (2018). Doctoral Dissertations. 1176. https://scholarworks.umass.edu/dissertations_2/1176
- [36] Q. Huang, I. Yoon, J. Villanueva, K. Kim, D.J. Sirbulu, Quantitative mechanical analysis of thin compressible polymer monolayers on oxide surfaces, *Soft Matter*. 10 (2014) 8001-8010. doi:10.1039/c4sm01530d.
- [37] J. Israelachvili, The different faces of poly(ethylene glycol), *PROC. NATL. ACAD. SCI. U. S. A.* 94 (1997) 8378-8379
- [38] S.H. Behrens, D.G. Grier, The charge of glass and silica surfaces, *J Chem Phys.* 115 (2001) 6716-6721.
- [39] X. Chen, M.C. Davies, C.J. Roberts, S.J.B. Tendler, P.M. Williams, N.A. Burnham, Optimizing phase imaging via dynamic force curves, *Surf Sci.* 460 (2000) 292-300.
- [40] A.B. Witte, A.N. Leistra, P.T. Wong, S. Bharathi, K. Refior, P. Smith, O. Kaso, K. Sinniah, S.K. Choi, Atomic force microscopy probing of receptor-nanoparticle interactions for riboflavin receptor targeted gold-dendrimer nanocomposites, *J Phys Chem B.* 118 (2014) 2872-2882.
- [41] P. Lemoine, J.P. Quinn, P.D. Maguire, J.F. Zhao, J.A. McLaughlin, Intrinsic mechanical properties of ultra-thin amorphous carbon layers, *Appl Surf Sci.* 253 (2007) 6165-6175.
- [42] A.K. Bhattacharya, W.D. Nix, Analysis of elastic and plastic deformation associated with indentation testing of thin films on substrates, *Int. J. Solids Struct.* 24 (1988) 1287-1298.
- [43] A.M. Korsunsky, M.R. McGurk, S.J. Bull, T.F. Page, On the hardness of coated systems, *Surf. Coat. Technol.* 99 (1998) 171-183.
- [44] R. García, R. Pérez, Dynamic atomic force microscopy methods, *Surf Sci Rep.* 47 (2002) 197-301.
- [45] T. Uchihashi, M. Higgins, Y. Nakayama, J.E. Sader, S.P. Jarvis, Quantitative measurement of solvation shells using frequency modulated atomic force microscopy, *Nanotechnology*. 16 (2005) S49-S53.
- [46] F. Gramazio, M. Lorenzoni, F. Pérez-Murano, L. Evangelio, J. Fraxedas, Quantification of nanomechanical properties of surfaces by higher harmonic monitoring in amplitude modulated AFM imaging, *Ultramicroscopy*. 187 (2018) 20-25.
- [47] M. Damircheli, A.F. Payam, R. Garcia, Optimization of phase contrast in bimodal amplitude modulation AFM, *Beilstein J. Nanotechnology*. 6 (2015) 1072-1081.

Ligand	Molecular structure
PEG-SH (MW=5000 g/mol)	
RME-peptide (MW=2083 g/mol)	CKKKKKKSEDEYPYVPN

sample	D _H , nm (DLS)	ζ potential, mV (ELS)
CC:AuNP	17.40 ± 0.20	-30.65 ± 1.5
PEG-SH:AuNP	37.29 ± 0.37	-6.74 ± 0.5
MM-RME:AuNP	38.23 ± 0.90	-4.4 ± 0.2

Table 1: Labelling, molecular structure of ligands and properties of AuNP. The amino-acid residues are labelled with the amino acid one letter code. D_H is the hydrodynamic diameter measured from dynamic light scattering and the ζ potential is measured from electrophoretic spectroscopy.

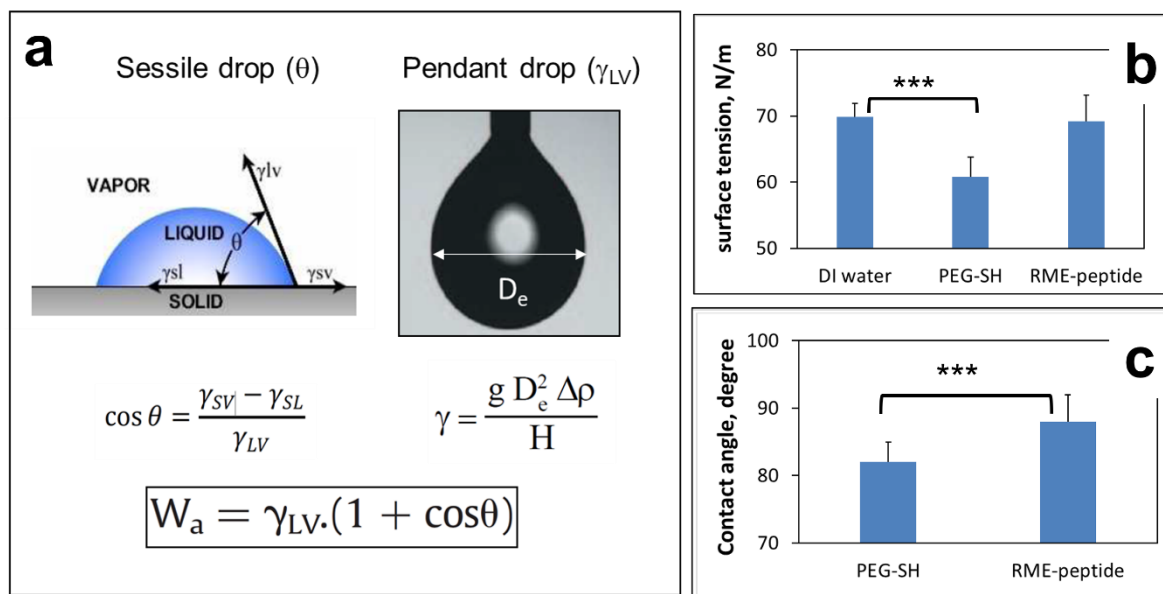


Figure 1: Contact angle and pendant drop experiments for the ligand solutions : a) schematics and equations, b) surface tension results and c) contact angle results on the gold surface.

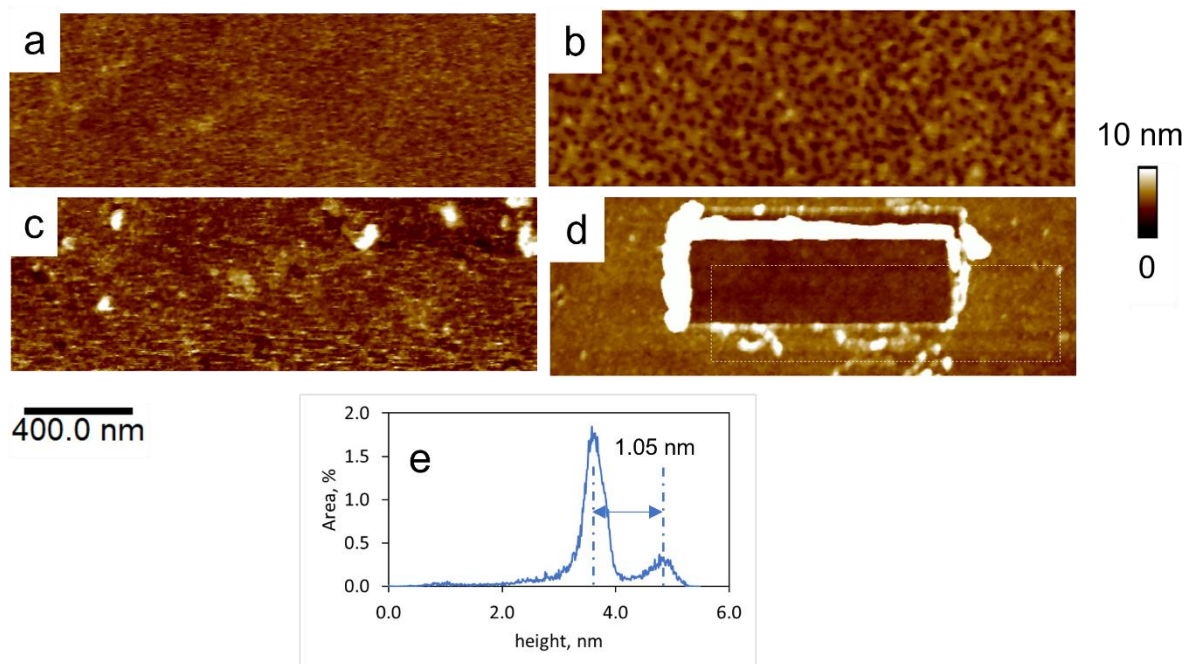


Figure 2: TAFM height images in air of ligand layers from dilute solutions ($7 \mu\text{M}$): a) gold substrate, b) PEG-SH 8hrs, c) RME-peptide 8hrs, d) RME-peptide 8 hrs with scratched area, e) Height histogram from d) showing 1.05 nm step height. The 400 nm scale bar and 10 nm height scale are for all images.

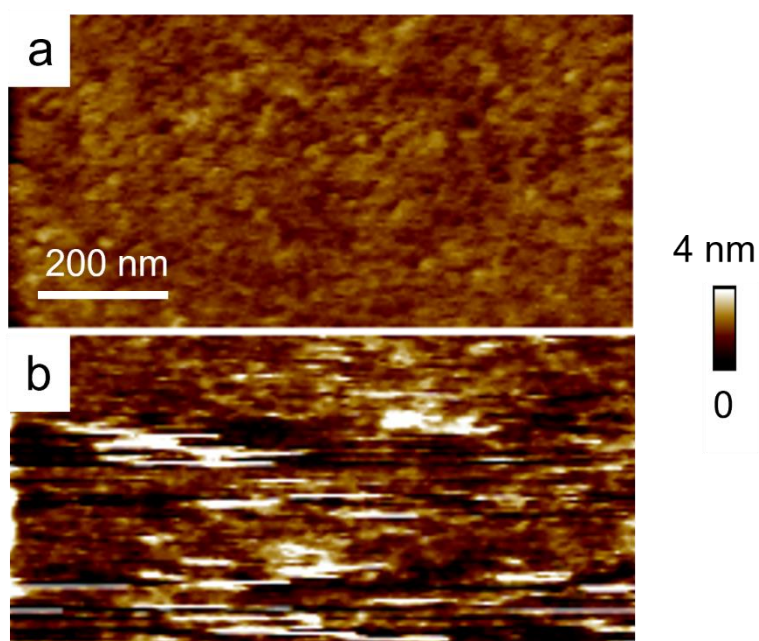


Figure 3: $1 \mu\text{m}$ CAFM height images in DI water of ligand layers from concentrated solutions ($0.2 \mu\text{M}$): a/ PEG-SH ($R_q = 0.30 \text{ nm}$) and b/ RME-peptide ($R_q = 1.63 \text{ nm}$). 200 nm marker bar and 4 nm high scale are the same for both images.

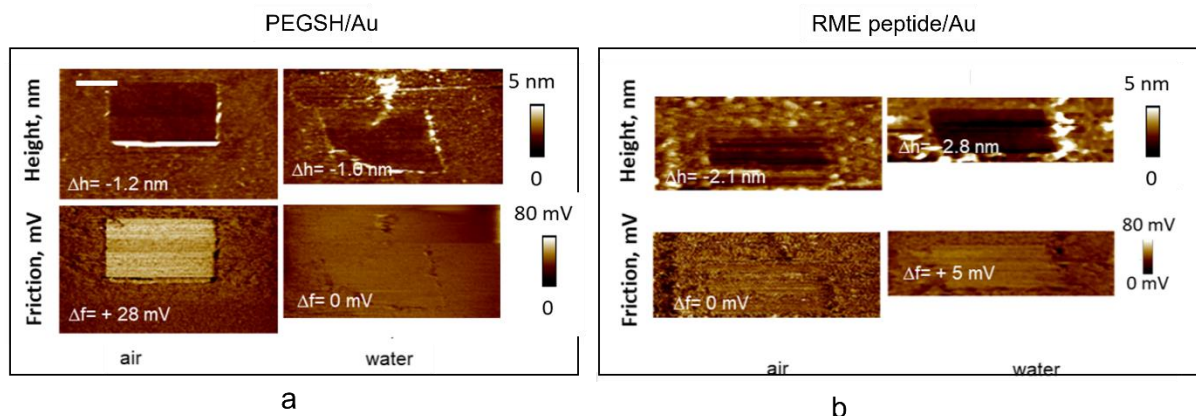


Figure 4: 2 μ m CAFM height and friction images of ligand layers from concentrated solutions (0.2 μ M) obtained in air and in DI water: a/ PEG-SH and b/ RME-peptide. The contrast between the scratched and unscratched area is shown in the images for the height (Δh) and friction (Δf) signals. Scale bar, shown for all image is 400 nm.

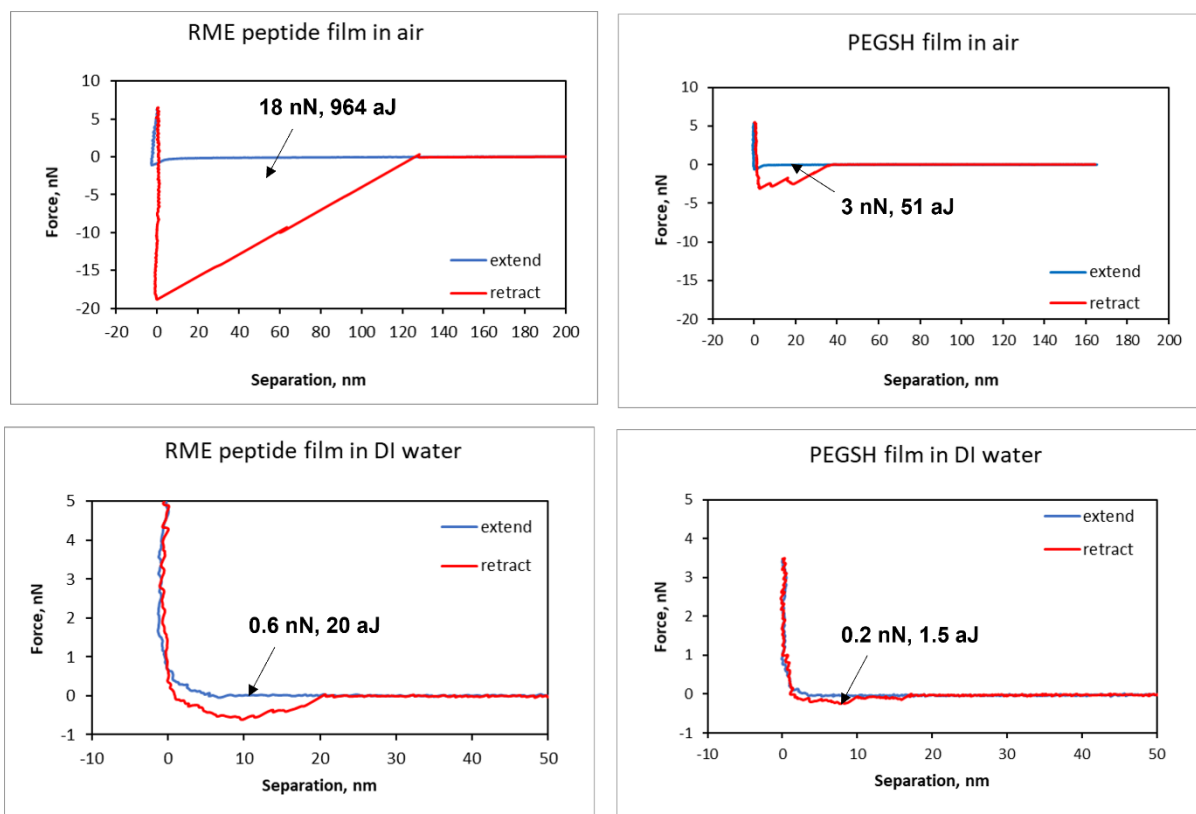


Figure 5: Average AFM force-separation curves in air and in DI water for ligand films on gold; RME peptide and PEGSH obtained in air and in DI water prepared at 200 μ M. The adhesion pull-off force (in nN) and energy dissipation (in aJ) are also shown in the curves.

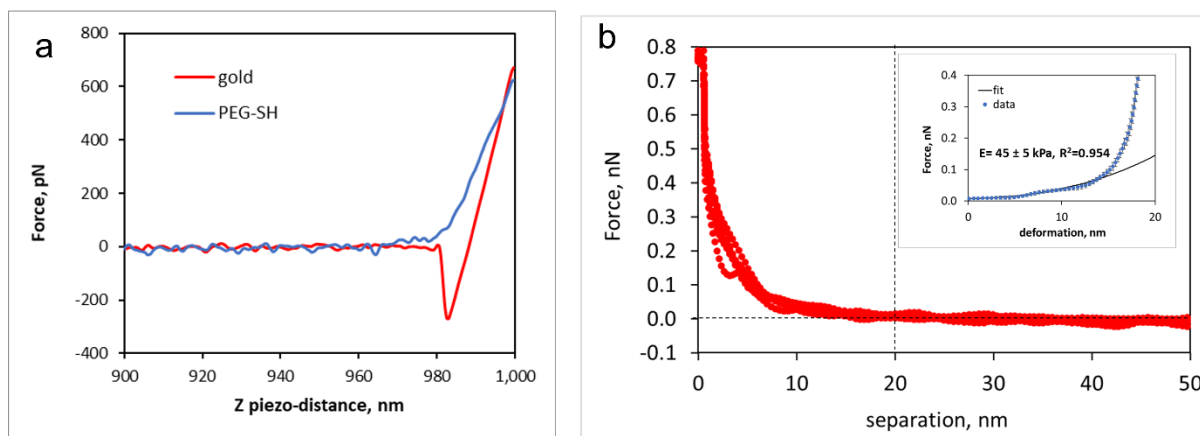


Figure 6: a/ Force curves obtained in DI water at low force for gold and the PEGSH film prepared at 200 μM , b/ Force separation curves and, insert, force-indentation curve with fit of the Dimitriadis model (ref 31) to take into account the substrate effect. The calculated low Young modulus value is indicative of a film with low chain density and entanglements.

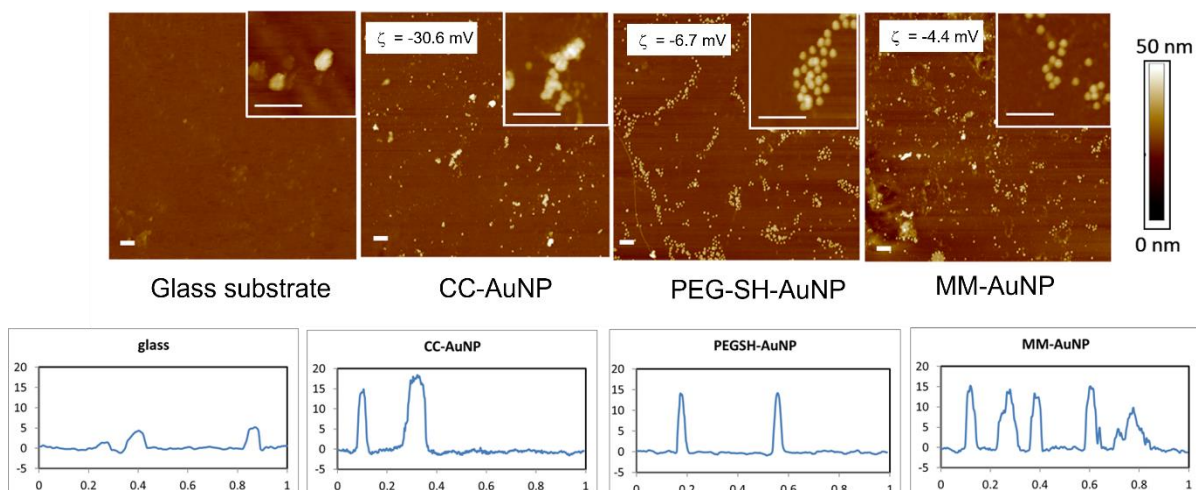


Figure 7: 4 μm TAFM images in air for of glass substrate and adsorbed AuNPs. Cross-sectional traces are shown below the images. Marker bar= 200 nm in both main images and inserts. The 1 μm cross-sections, all with a 25 nm vertical scale, are across significant features; i.e. contaminants for the glass, AuNP for the other samples.

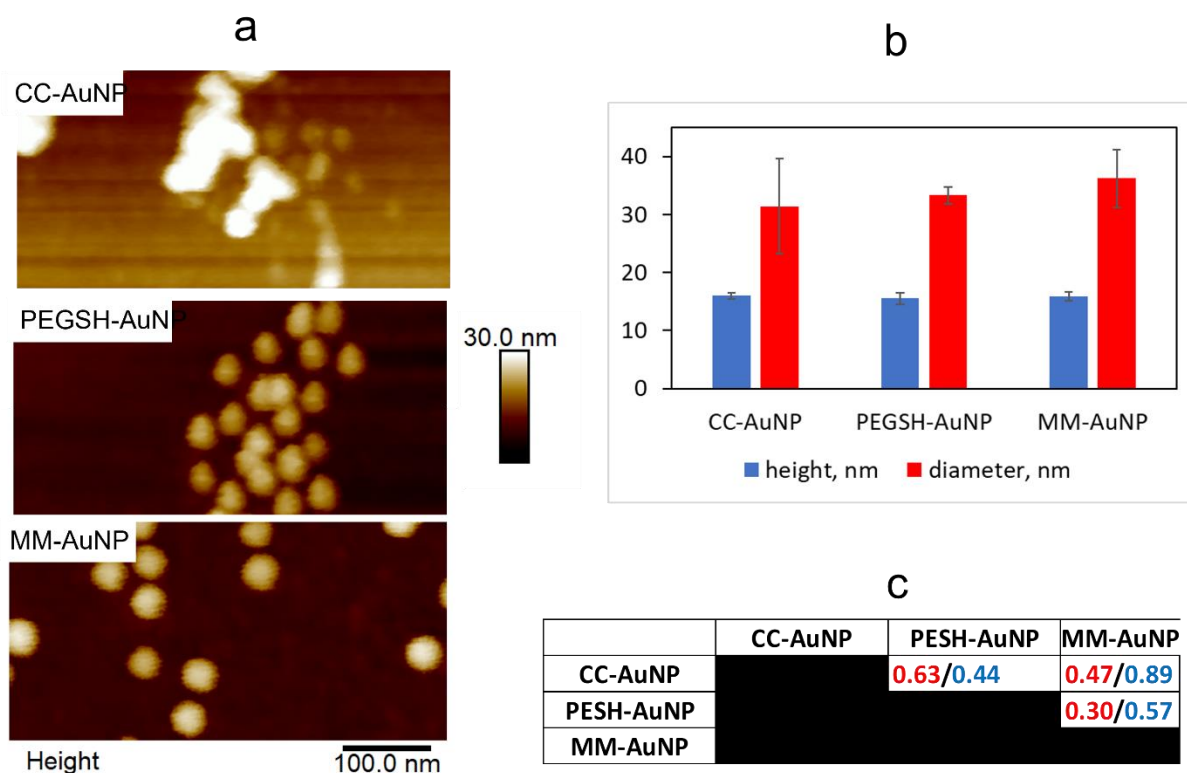


Figure 8: a/ 500nm TAFM images in air for CC-AuNP, PEGSH-AuNP and MM-AuNP adsorbed on glass obtained with optimised imaging conditions. b/ Corresponding histograms for particle heights and diameters and c/ table of student t-test p-values for 'pair comparisons', in red for diameter and blue for height, showing no statistical differences between the three samples (i.e. p-values > 0.05)

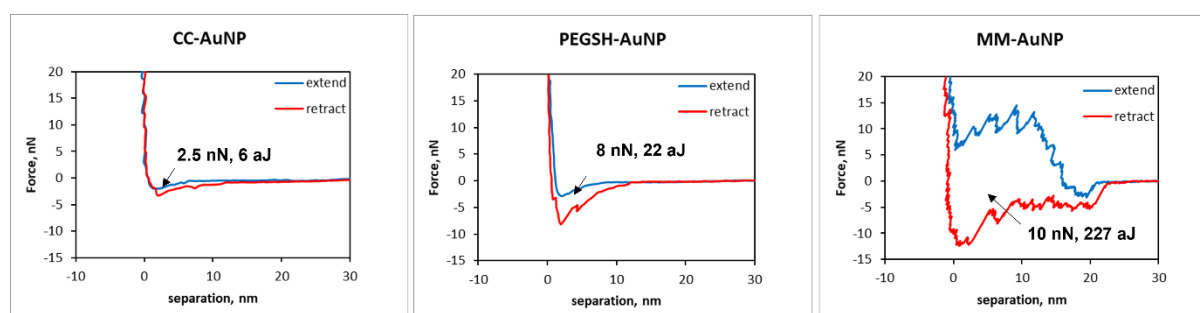


Figure 9: Representative AFM force-separation curves for CC-AuNP, PEGSH-AuNP and MM-AuNP